Electronic Supplementary Material (ESI) for Lab on a Chip.

Supporting information

Label-free single-cell isolation enabled by microfluidic impact printing and real-time cellular recognition

Yiming Wang[a, b], Xiaojie Wang[a, b], Tingrui Pan[a, c], Baoqing Li*[a, b], Jiaru Chu[a, b]

[a.] *Department of Precision Machinery and Precision Instrumentation, University of Science and Technology of China, Hefei, Anhui, China, 230027*

[b.] *Key Laboratory of Precision Scientific Instrumentation of Anhui Higher Education Institutes, University of Science and Technology of China, Hefei, Anhui, China, 230027*

[c.] *Suzhou Institute for Advanced Research, University of Science and Technology of China, Suzhou, 215123, China*

*Electronic mail: bqli@ustc.edu.cn

1. System setup

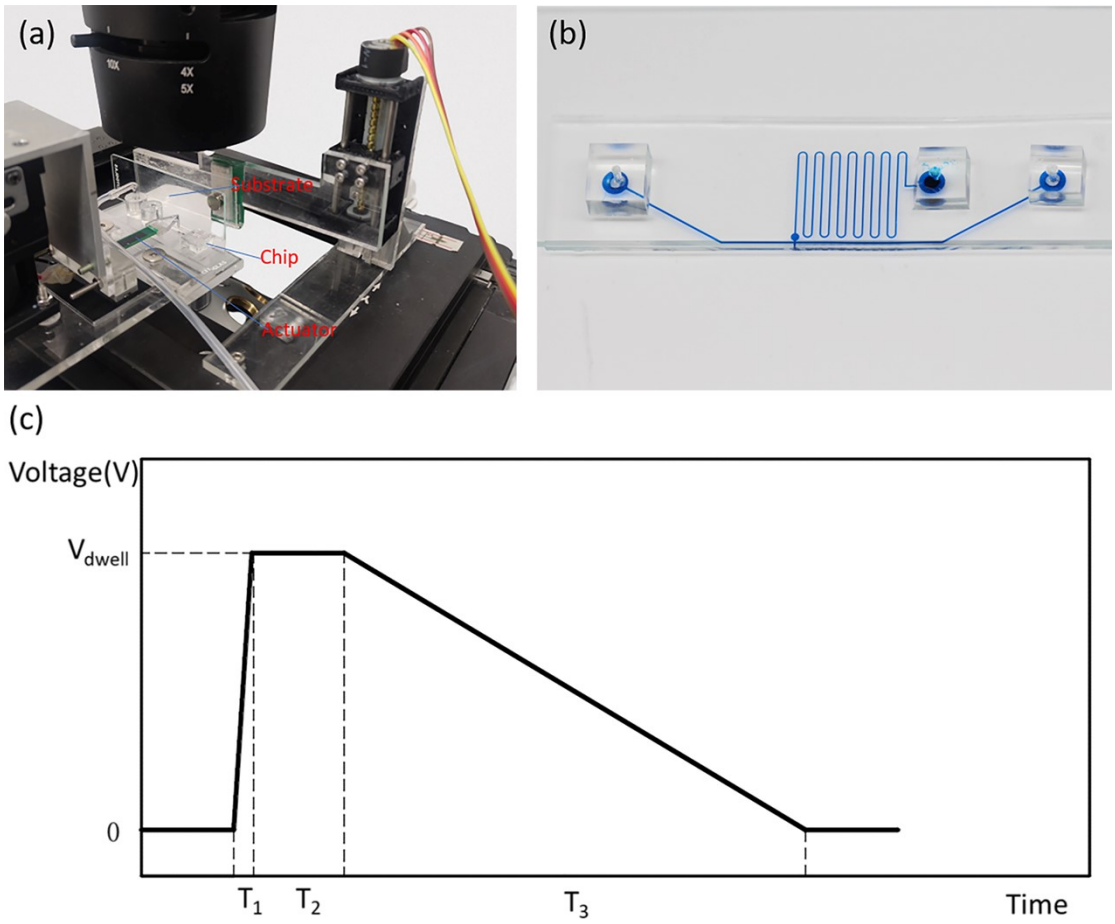

Fig. S1. Experimental setup of the microfluidic single-cell isolation system. Images of (a) the printing module, and (b) the microfluidic chip. (c) Schematic diagram of the trapezoidal waveform used for droplet generation. T_1 is the rise time of the piezoelectric actuator extending to the bottom of microchannel at high velocity, which was as short as 2 μs. T_2 is a dwell time of 1 ms to avoid the piezoelectric actuator shaking. T_3 is a fall time of 5 ms for preventing gas from being sucked into the chip.

2. Simulation of cell flow and single-cell droplet generation

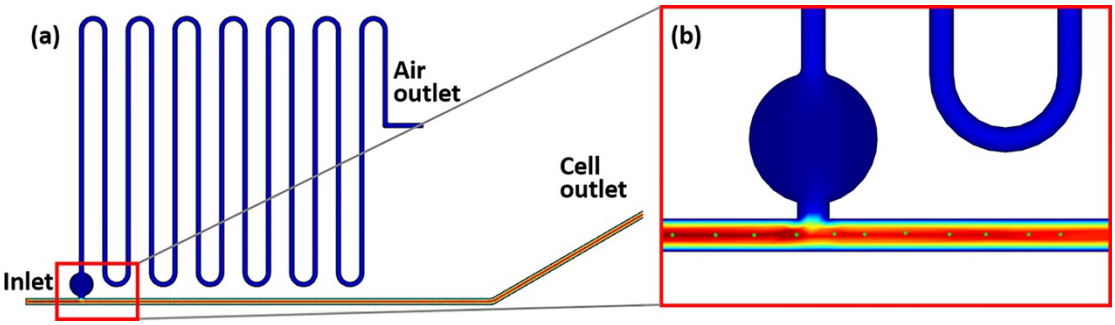

Fig. S2. Simulation of cell tracking and the flow velocity distribution when the cells flow from the inlet. (a) Simulation model. (b) Flow velocity distribution of the flow field and cell trajectory. Red represents a high flow velocity, blue a low rate. Green spots represent cells.

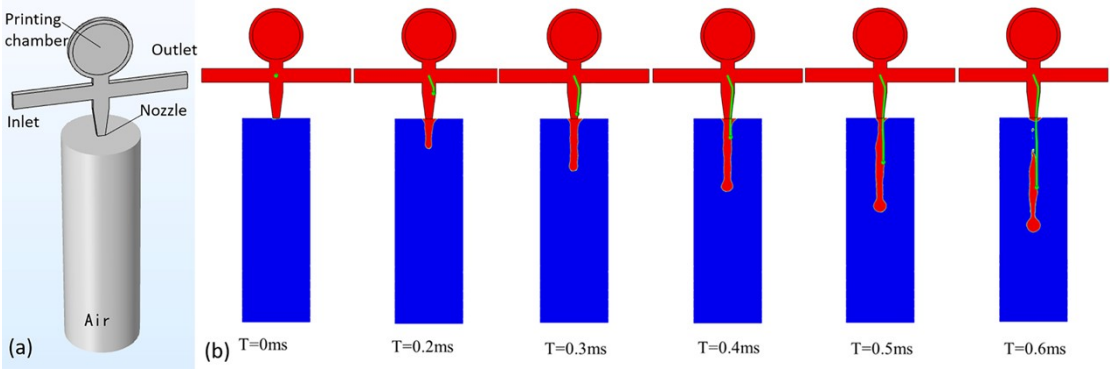

Fig. S3. Simulation of droplet generation. (a) Two-phase geometry model consisting of an inlet, an outlet, a nozzle, a printing chamber, microchannels, an air cylinder and a bead. The inlet and outlet are simplified as the equivalent pressure within the liquid phase; the vent section between printing chamber and air outlet is ignored because its high resistance to flow has no effect on droplet generation. The simulation fluid is water at 25°C. The bead is driven by the fluid at a flow velocity of 10 mm/s. (b) Simulation results of droplet generation at different time points from 0–0.6 ms. Red represents water, the green spot represents a bead, while blue represents air. Bead tracking is marked by a green line. The droplet volume is calculated using an integral function.

3. Image processing and threshold choose

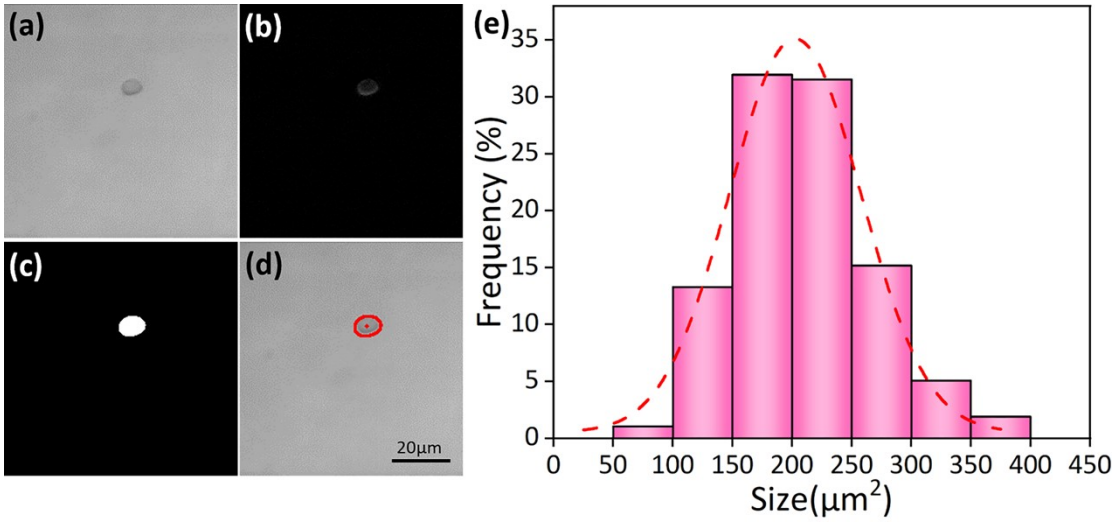

Fig. S4. Image processing steps for single cells, and the size distribution of HeLa cells. (a) Original image captured by a high-speed camera. (b) The resulting image after applying background subtraction. (c) A binary image generated using threshold segmentation. (d) The contour and center of the cell were extracted by a contours-finding function and marked by a red line and spot, respectively. (e) Frequency distribution of cell sizes.

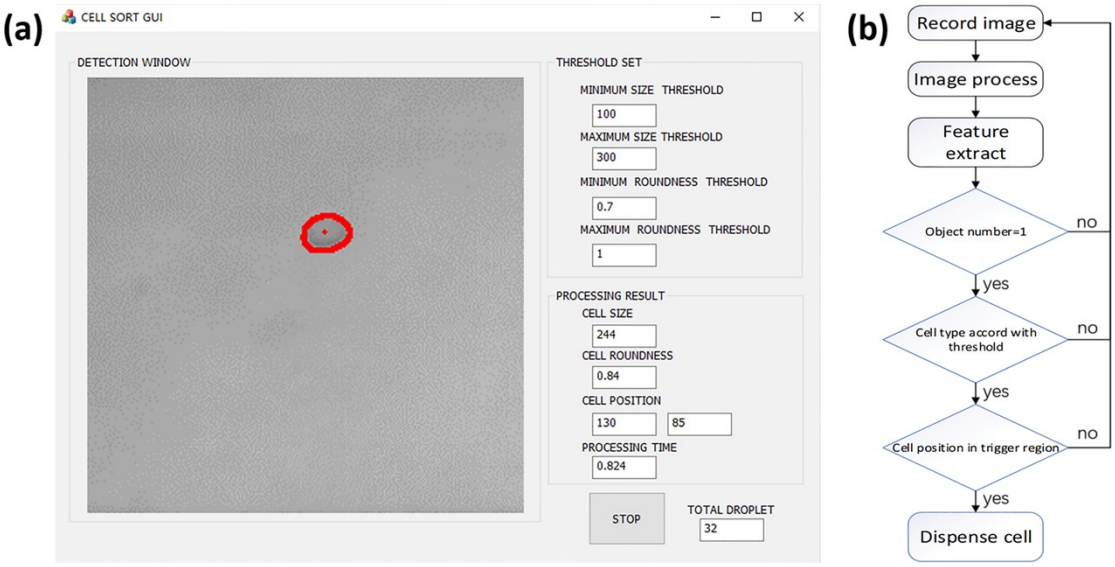

Fig. S5. Graphical User Interface (GUI) and flowchart for cell dispensing. (a) A GUI programmed by C++ allows the user to set thresholds of size and roundness for selection of specific cells. The detection zone is shown in the GUI. (b) The flowchart shows the implementation of the cell detection algorithm.

To show the trade-off of the printing system, four sorting thresholds, marked by dashed line in Fig.S6a, are chosen to study the relationship between yield and threshold. Yield is defined as the ratio of the number of targets in the selected threshold and the number of whole targets that flow through the microchannel, and the cell waste is defined as the ratio of the number of targets out of the selected threshold and the number of whole targets that flow through the microchannel. As shown in Fig. S6b, when the threshold increases, the yield increases, which means the cell waste decreases.

Recognition accuracy is defined as the ratio of the number of single cells in the selected threshold and the number of targets in the selected threshold. It can also be seen from Fig.S6b that the recognition accuracy decreases with threshold increasement. Table S1 quantitatively describes this trade-off for HeLa cells.

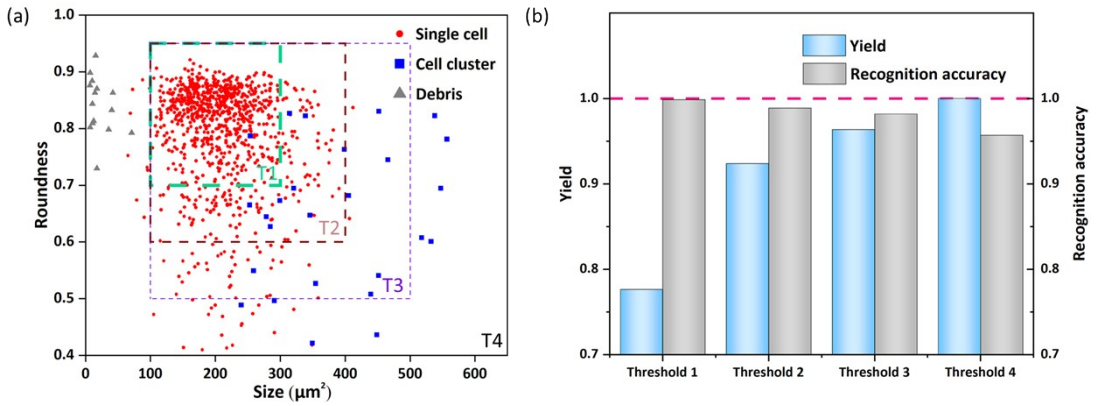

Fig. S6. (a) A roundness-size scatter plot of 1000 HeLa cells captured in the detection zone, and manually classified as single cells, cell clusters, or debris. The four sorting thresholds are indicated by dashed line. T4 represents threshold 4, which means that the whole targets are in the threshold region. (b) The yield and recognition accuracy with different thresholds.

Table S1. The printing performance of different threshold

Threshold	Yield	Recognition accuracy	Single cell efficiency	the number of cells required
Threshold 1	77.6%	99.9%	90.3%	1427
Threshold 2	92.4%	98.9%	89.4%	1211
Threshold 3	96.3%	98.2%	88.8%	1169
Threshold 4	100%	95.7%	86.5%	1156

Moreover, we can estimate the number of cells required in the original sample for getting a thousand single-cell droplets from Fig. S6b. As shown in Table S1, in the range of the threshold 1, 1427 cells are need to acquire 1000 single-cell droplets. The number of cells required in the original sample is smaller with larger threshold, but the single cell efficiency is declined due to the lower recognition accuracy.

4. Simulation of bead motion

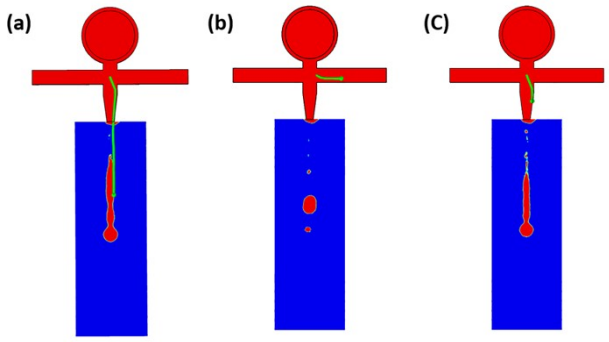

Fig. S7. Three simulation results of bead motion during droplet generation using different boundary conditions. Red represents water and blue represents air. Green spots represent beads. (a) Bead is ejected with the droplet. (b) Cell travels laterally due to the position of cell out of the trigger region. (c) Bead travels forward due to a lower droplet volume. Its displacement of the printing chamber is lower than the others as a result of a lower driving voltage.

5. Study of the inherent bias in the printed cells

In order to study the inherent bias in the cells which are successfully printed, single cells were printed into a microwell plate containing complete culture medium and were cultured for 12 hours. As shown in Fig. S7a, microscope images of the cells are captured and the nuclear area and aspect ratio of the printed cells are calculated by ImageJ. The wasted cell and the cells obtained by serial dilution are treated as control group, as shown in Fig. S7b and Fig. S7c. The result is shown in Fig. S7d. The aspect ratio of the cells is represented by roundness. It can be concluded that there is no inherent bias in the cells which are successfully printed.

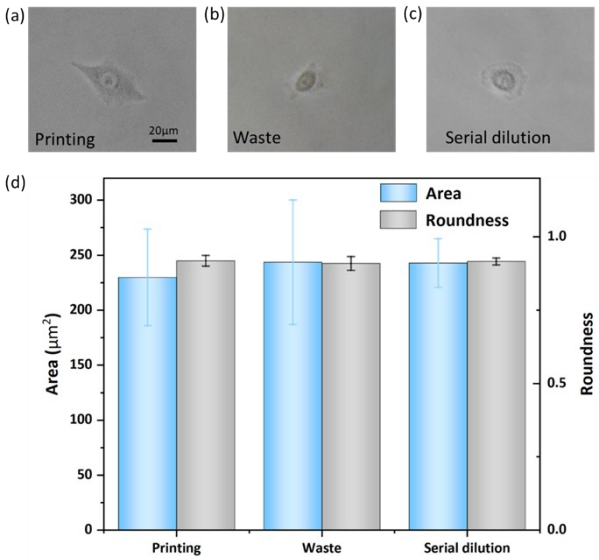

Fig. S8. The study of inherent bias in the cells. Microscope images of a sorted cell (a), a waste cell (b) and a cell obtained by serial dilution (c) after 12 hours growth. (d) Nuclear area and nuclear roundness of the printed cells, wasted cells, and the cells obtained by serial dilution. Each condition is quantified with 10 cells.

6. Design of the device

The schematic of the geometry of the microfluidic chip is shown in Fig. S9 and the parameter of our chip is shown in Table S2. H is the height of the chip, it is chosen as 75 μm according to our previous works [1, 2], which is a suitable parameter to generate a droplet at a stability way. W_1 is the width of microchannel. W_2 is width of the detection zone. We chose it as 200 μm × 200 μm according to Goda's work[3-5], because 200 μm is suit for most cells, even those large cells.

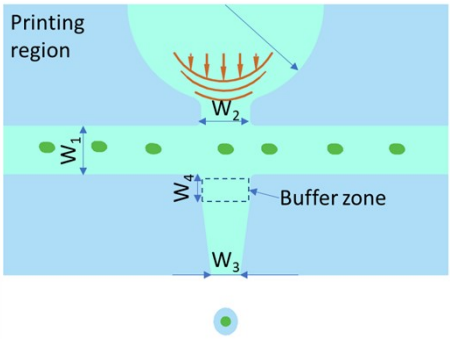

Fig. S9. The schematic of the geometry of printing region.

Table S2. the parameter of printing region of microfluidic chip.

Name	Size(μm)	Explain
R	300	Radius of printing chamber
W_1	200	Width of the channel
W_2	200	Width of the detection zone
W_3	120	Width of the nozzle
W_4	100	Width of the buffer zone
H	75	Height of the chip

W_3 is the width of nozzle**.** There are several principles to choose the width of nozzle as following:

(1) The length of single Hela cell is about 20 μm and the length of Hela cell cluster is about 40 μm. Therefore, the width of the nozzle should larger than 40μm to prevent nozzle clogging. We can conclude that:

$$W_3 \geq 40\mu m \tag{S1}$$

(2) To prevent the liquid from flowing out of the nozzle, the pressure P_2 at the nozzle should be smaller than the surface tension of the nozzle. According to the surface tension equation, it can be expressed as:

$$P_2 \leq \frac{4\gamma cos\sigma}{D_e} \tag{S2}$$

where γ is the surface tension of the air–liquid interface, σ is the contact angle between the printing material and the wall of the microchannel, D_e is the hydraulic equivalent diameter of nozzle, respectively. P_2 is the pressure of the nozzle, as shown in Fig. S10. Meanwhile, P_1, P_2', P_3, P_4 are represented the pressure of inlet, channel crossing, waste outlet and air outlet, respectively. Q_1, Q_2, Q_3 are represented the volumetric flow rate of each section.

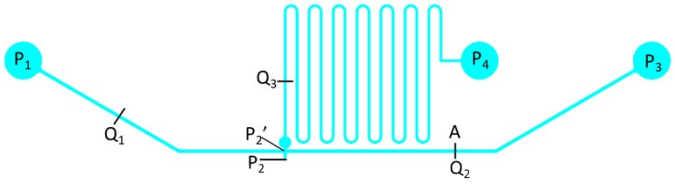

Fig. S10. The schematic of the geometry of the microfluidic chip.

When the actuator doesn't work, there is no liquid flowing out of the nozzle. In the condition of low-speed laminar flow (Re<100), it is assumed that the pressure of nozzle is similar to the pressure of the channel crossing, we can conclude:

$$P_2 \approx P_2^{'} \tag{S3}$$

According to the Hagen–Poiseuille equation[6], the relationship between the volumetric flow rate Q_2 and the pressure at nozzle P_2 and waste outlet P_3 can be expressed as:

$$Q_2 = \frac{P_2 - P_3}{R_2} \tag{S4}$$

$$R_2 = \frac{12\eta L\alpha}{H^4(1 - 0.63\alpha)} \tag{S5}$$

where R_2 is the flow resistance between the channel crossing and waste outlet, η is the viscosity of water, *L* is the length between the channel crossing and the waste outlet of the microchannel, α is the aspect ratio of the microchannel ($\alpha=H/W_1$), respectively.
The waste outlet and air outlet are connected to the atmosphere. Therefore, we can conclude:

$$P_3 = P_4 = 0 \tag{S6}$$

The serpentine channel connected to the air outlet is designed to have a longer length and larger flow resistance than the straight channel connected to the waste outlet ($R_3 >> R_2$, as shown in Table S3). Therefore, the volumetric flow rate Q_3 is much smaller than Q_2. Therefore, we can conclude:

$$Q_1 \approx Q_2 \tag{S7}$$

By substituting equations (S3), (S4), (S6) and (S7) into equation (S2), the relationship between the volumetric flow rate Q_1 and the hydraulic equivalent diameter of nozzle D_e can be expressed as:

$$Q_1 \leq \frac{1}{D_e} \cdot \frac{4\gamma cos\sigma}{R_2} \tag{S8}$$

Then, the average flow velocity in the microchannel between inlet and nozzle can be calculated by:

$$v_{av} \leq \frac{Q_1}{A} = \frac{1}{D_e} \cdot \frac{4\gamma cos\sigma}{A \cdot R_2} \tag{S9}$$

where A is the cross-section area of the microchannel ($A=H \cdot W_1$).
Therefore, the maximum flow velocity in the center of microchannel can be calculated by:

$$v_{max} \leq 2v_{av} = \frac{1}{D_e} \cdot \frac{8\gamma cos\sigma}{A \cdot R_2} \tag{S10}$$

It means that the hydraulic equivalent diameter of nozzle is determined by the maximum flow velocity of particles:

$$D_e \leq \frac{1}{v_{max}} \cdot \frac{8\gamma cos\sigma}{A \cdot R_2} \tag{S11}$$

Parameter values in the equations are shown in Table S3, equation (S11) can be calculated:

$$D_e \leq \frac{1.40 \times 10^{-6}\, m^2 \cdot s}{v_{max}} \tag{S12}$$

From this equation, we can conclude that the equivalent diameter increases while the maximum flow velocity decreases. The maximum flow velocity is also verified by experiments, the results of which are summarized in Fig. S11. In experiment, the flow velocity of bead in the center of microchannel is measured by the high-speed camera under the maximum pressure that the nozzle can sustain, and is regard as the maximum flow velocity. The theoretical calculations (red line) and experimental results (blue points) show that the maximum flow velocity is significantly affected by nozzle size, and exhibits an inverse correlation. Although the experimental results are basically consistent with the theoretical results, the experimental results have a greater decline than the

theoretical results with the increase of nozzle size. It may be caused by the approximation in equations (S3) and (S7).

Table S3. Parameter values in the equations.

Name	value	Explain
ρ	1000 kg/m^3	Density of printing chamber
A_d	9000 μm^2	Cross-section area of the nozzle
γ	0.0728 N/m	Surface tension factor of water
σ	120°	Contact angle of PDMS and water (After hydrophobic process)
L	25 mm	Length between the channel crossing and the waste outlet
η	0.00298 Pa·s	Height of the chip
α	0.375	Aspect ratio of the microchannel
A'	282743 μm^2	Area of the pin
v_{av}	5 mm/s	Average flow velocity of particles
P_2	1040 Pa	Pressure of the nozzle
A	15000 μm^2	Cross-section area of microchannel
R_2	1.387×10^{13} Pa·s·m^{-3}	Flow resistance between the channel crossing and waste outlet
R_d	4.505×10^{11} Pa·s·m^{-3}	Flow resistance between the channel crossing and nozzle
R_1	9.986×10^{12} Pa·s·m^{-3}	Flow resistance between the inlet and the channel crossing
R_3	9.899×10^{13} Pa·s·m^{-3}	Flow resistance between the channel crossing and the air outlet

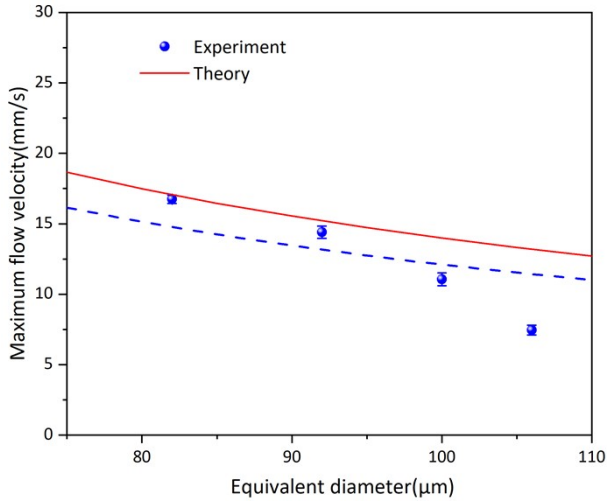

Fig. S11. Relationship between nozzle's equivalent diameter and maximum flow velocity.

From above analysis, the nozzle's equivalent diameter is related to the maximum flow velocity. Therefore, we should choose the maximum flow velocity first. The small flow velocity means the low throughput, so we expect to apply a higher flow velocity. However, when the flow velocity of cells increases, the travel distance of the cells caused by image transmission and processing will increase. It will result in incorrect printing of particles and reduces the efficiency of single cell. In this work, the flow velocity of 10mm/s is appropriate. The travel distance of the cells was about 12.5 μm, calculated from the flow velocity (10 mm/s) and the trigger latency (1.25 ms), which is much smaller than the width of the detection zone (200 μm).

According to Fig. S11, the corresponding equivalent nozzle diameter of 10 mm/s flow velocity is about 100 μm. The width of the nozzle W_3 can be calculated by:

$$D_e = \frac{2W_3H}{W_3 + H} \tag{S13}$$

The corresponding width of the nozzle W_3 is 150 μm. We can conclude that width of the nozzle should meet equation (S14) with 10mm/s flow velocity:

$$40\mu m \leq W_3 \leq 150\mu m \tag{S14}$$

(3) The bigger of the ratio of nozzle size and particles size means more stability for particles ejection[7]. The nozzle should as big as possible for printing cells out of the nozzle.

In the end, in order to prevent the pressure fluctuation from causing the cells to flow out of the nozzle, a smaller nozzle width W_3 is chosen as 120 μm in this work.

W_4 is the width of the buffer zone of the nozzle. The buffer zone of the nozzle is shown in Fig. S9. If there is no buffer area, the nozzle is too close to the printing chamber, the air will be sucked into the printing chamber when the actuator is drawback, and then the printing system will become unstable. As shown in Fig. S12a-d, a microfluidic chip without buffer zone is used to demonstrate this phenomenon. At 0 ms, the piezoelectric actuator generates an impact force to push the liquid toward the nozzle, and then a droplet is dispensed. Subsequently, when the piezoelectric actuator is withdrawn, air is aspirated from the nozzle to the printing chamber (T=2 ms). The bubble is trimmed by the flow shear force (T=3 ms). The air in the nozzle is pushed out of the nozzle quickly, but the other air is sucked into the printing chamber.

To address this, we add the buffer zone to ensure the air does not enter the print chamber. Experimental results demonstrate that the buffer length of 400 μm can completely prevent the suction back to the printing chamber, as shown in Fig. S12e. However, the longer distance of buffer zone increases the chance of the cells bumping into the wall. We establish a finite element method (FEM) simulation to explain this phenomenon. As shown in Fig. S13, the droplet volume is 12.3 nL in the simulation, and the corresponding nozzle volume is only 11.1 nL. The nozzle volume is defined as the surface area of the nozzle (as shown in Fig. S14a) times the depth of the channel. The bead is in the center of the trigger region, it should be ejected in theory. However, it bounces the wall of nozzle and its velocity decrease. For the increase of travel distance in the buffer zone, the bead cannot eject successfully with the droplet.

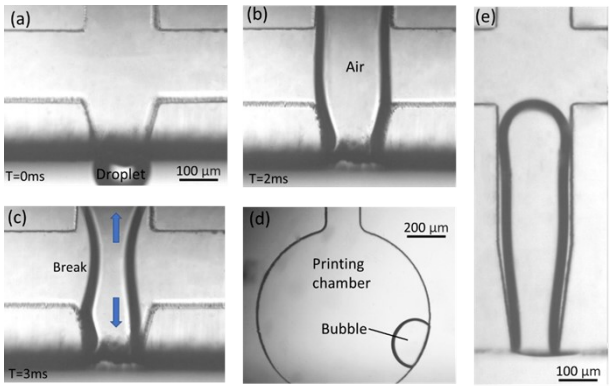

Fig. S12. The process of microfluidic impact printing without buffer zone captured by a high-speed camera.

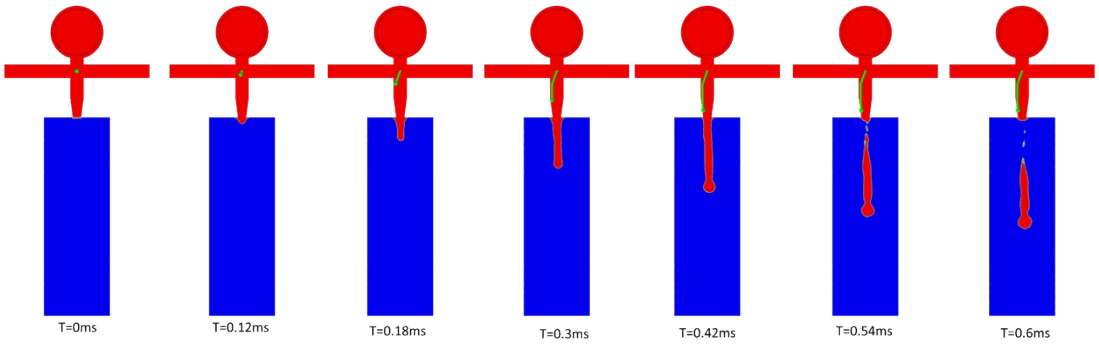

Fig. S13. The simulation result of bead motion during droplet generation with a 300 μm width buffer zone. Red represents water and blue represents air. Green spots represent beads. Bead tracking is marked by a green line.

At the same time, we adapt a waveform optimization to address this problem. The piezoelectric beam slowly withdraws with an optimized waveform, as shown in Fig. S1c and Fig.2. Under the pressure of capillary force and inlet, most of the suction will be offset during the withdrawal. However, there is another problem that the waveform optimization leads to long waiting time and reduces the throughput of printing.

In this work, we adapt a length of buffer zone of 100 μm and a waveform delay of 5 ms. From Fig.2, we can conclude that most cells can be ejected out of the nozzle and the air will not be suck into the printing chamber. Meanwhile, the waveform delay will not reduce the throughput in experiment.

D is the diameter of printing chamber**.** To expel the cells out of the nozzle, the displacement volume of printing (V) chamber should larger than the droplet volume (V_d). And the droplet volume (V_d) should be at least equal to the nozzle volume (V_n) to ensure the cell is encapsulated in the droplet (as we demonstrated in main article). Therefore, the displacement volume (V) of printing chamber should larger than the nozzle volume (V_n). As shown in Fig. S14b, the deformation of the PDMS microchannel can be simplified as a truncated cone. The displacement volume is marked by the section line and is calculated by the volume formula of truncated cone:

$$V = \frac{1}{12}\pi h(D^2 + D'^2 + D \cdot D') \tag{S15}$$

where D is the diameter of the printing pin, D′ is the diameter of the printing chamber, h is the displacement of the piezoelectric actuator, it increases linearly with driving voltage and can be calculated by Fig. S14a.

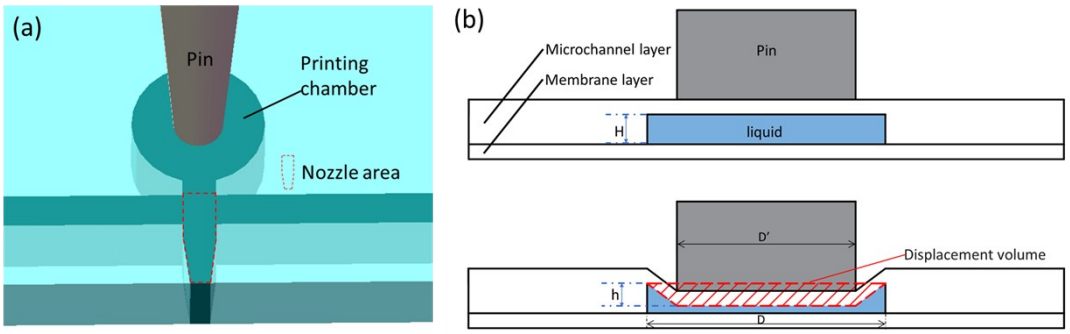

Fig. S14. Analytical model of membrane deformation. (a) Top view of a membrane pump. (b) Cross-sectional view of the deformation model during driving of a membrane pump.

In this work, we apply a 600 μm diameter of the printing pin and an 800 μm diameter of the printing chamber. The printing chamber is larger than the printing pin for setting up. The maximum displacement of the piezoelectric actuator is 75 μm (equal to the height of microchannel). According to equation (S15), the maximum displacement volume of the microchannel is 21.2 nL, which is larger than the nozzle volume (8.1 nL in current work), and it is suitable to study the relationship between the droplet volume and printing efficiency by generating a series of volumetric gradients of droplets.

Selection and setup of the piezoelectric actuator. Piezoelectric actuators can be divided into piezoelectric beam, piezoelectric plate, and piezoelectric stack. Piezoelectric beam has large stroke, moderate impact force and low cost. The maximum displacement of piezoelectric plate is relatively small, and the size of piezoelectric plate is too large to package and clamp. The maximum displacement of piezoelectric stack is still smaller than piezoelectric beam and the cost is higher. Considering the separated modular design between the actuator and the chip in the microfluidic impact printing system, we choose the piezoelectric beam as the actuator in the microfluidic impact printing system in order to have a large assembly margin during the system construction and chip assembly.

There are two conditions that the piezoelectric beam need to meet, which are its velocity and displacement. The velocity of the piezoelectric actuators should satisfy the momentum equation to generate a droplet, it can be written as:

$$\rho A_d v_d \Delta t \cdot v_d = \left[2(H + W_3)\gamma cos\sigma - P_2 \cdot A_d\right] \cdot \Delta t \tag{S16}$$

where A_d is the area of the nozzle (A_d=H·W_3), v_d is the velocity of droplet in the nozzle, γ is the surface tension of the air–liquid interface, σ is the contact angle between the printing material and the wall of the microchannel, P_2 is the inner pressure at the nozzle.

According to equation (S4) and (S6), we can conclude:

$$P_2 = Q_2 \cdot R_2 = A v_{av} \cdot R_2 \quad \text{(S17)}$$

where Q_2 is the volumetric flow rate, R_2 is the flow resistance between the nozzle and waste outlet, A is the area of the cross area of microchannel, v_{av} is the average flow velocity of the cells (which is 5 mm/s in this work).

By substituting the parameter values (as shown in Table S2 and Table S3) into equation (S16), we can conclude that the minimum flow velocity of liquid to generate a droplet in the nozzle is:

$$v_d = \sqrt{\frac{2(H + W_3)\gamma cos\sigma - P_2 \cdot A_d}{\rho A_d}} = 0.733\ m/s \quad \text{(S18)}$$

According to the continuity equation of incompressible fluids, when the droplet flow out of the nozzle, the flow resistance of nozzle R_d is much smaller than the flow resistance of other section R_1, R_2, and R_3, as shown in Table S3. Thus, all liquid squeezed from the printing chamber can be assumed to flow to the nozzle, we can conclude that:

$$A_d v_d \approx A' v_{min}' \quad \text{(S19)}$$

where A' is the area of the pin, and v_{min}' is the velocity of the piezoelectric actuator.

It can be concluded that the minimum velocity of piezoelectric beam (also the velocity of pin) is:

$$v_{min}' = \frac{A_d v_d}{A'} == 23.3 \quad mm/s \quad \text{(S20)}$$

The selected piezoelectric actuator is piezoelectric beam (QDTE52, PANT Corp, China), and some major specifications and parameters are shown in Fig. S15. Those parameters are measure by a laser Doppler vibrometer in working condition. The displacement reaches 74 μm at 80 V, which is about equal to the height of microchannel (75 μm). The velocity reaches 29 mm/s at 40 V. The velocity and displacement of piezoelectric beam meet our require. When the voltage is greater than 40 V, the condition is satisfied. In fact, in the experiment, the 40 V voltage can generate droplet sometimes, and sometimes not. It may be caused by the pressure fluctuation. And a little liquid flow to the outlet and inlet.

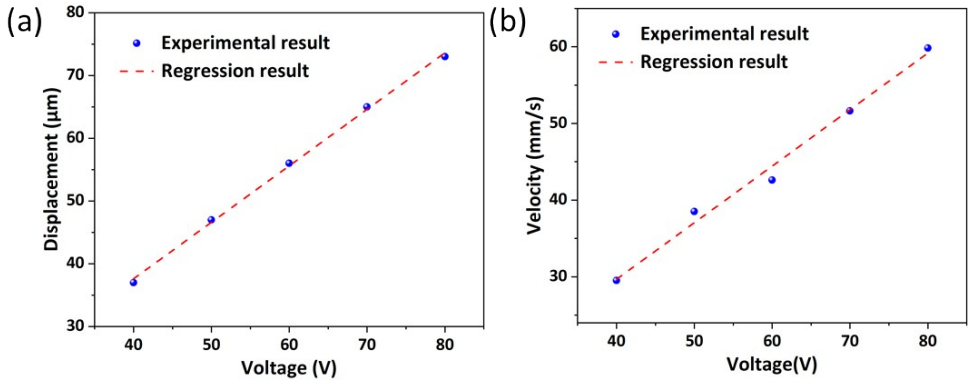

Fig. S15. The parameter of piezoelectric beam, which is measure by a laser Doppler vibrometer. (a) The relationship between the voltage and displacement. (b) The relationship between the voltage and velocity.

The set up of actuator and the printing chamber is shown in Fig. S16. One tip of the piezoelectric beam is connected to the XYZ triaxial mobile platform for adjusting the distance between the piezoelectric beam and chip, and the other tip is connected to a homemade resin part with a vetical pin. The homemade resin part is trasparent, which is benefit to oberseve the microchannel. The pin is aligned with the chip under the microscope.

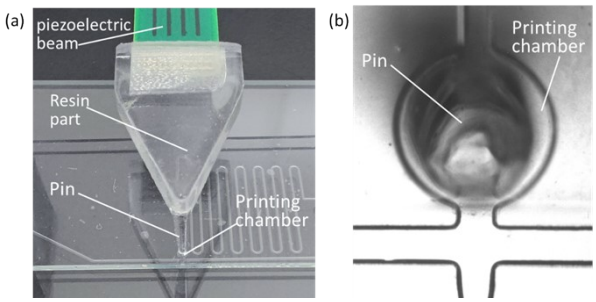

Fig. S16. The set up of actuator and the printing chamber.

References

1. Y. Mao, Y. Pan, X. Li, B. Li, J. Chu and T. Pan, *Lab Chip*, 2018, **18**, 2720-2729.
2. Y. Mao, X. Wang, X. Li, B. Li and J. Chu, *Journal of Micromechanics and Microengineering*, 2019, **29**.
3. A. Isozaki, H. Mikami, K. Hiramatsu, S. Sakuma, Y. Kasai, T. Iino, T. Yamano, A. Yasumoto, Y. Oguchi, N. Suzuki, Y. Shirasaki, T. Endo, T. Ito, K. Hiraki, M. Yamada, S. Matsusaka, T. Hayakawa, H. Fukuzawa, Y. Yatomi, F. Arai, D. Di Carlo, A. Nakagawa, Y. Hoshino, Y. Hosokawa, S. Uemura, T. Sugimura, Y. Ozeki, N. Nitta and K. Goda, *Nat Protoc*, 2019, **14**, 2370-2415.
4. S. Sakuma, Y. Kasai, T. Hayakawa and F. Arai, *Lab Chip*, 2017, **17**, 2760-2767.
5. N. Nitta, T. Sugimura, A. Isozaki, H. Mikami, K. Hiraki, S. Sakuma, T. Iino, F. Arai, T. Endo, Y. Fujiwaki, H. Fukuzawa, M. Hase, T. Hayakawa, K. Hiramatsu, Y. Hoshino, M. Inaba, T. Ito, H. Karakawa, Y. Kasai, K. Koizumi, S. Lee, C. Lei, M. Li, T. Maeno, S. Matsusaka, D. Murakami, A. Nakagawa, Y. Oguchi, M. Oikawa, T. Ota, K. Shiba, H. Shintaku, Y. Shirasaki, K. Suga, Y. Suzuki, N. Suzuki, Y. Tanaka, H. Tezuka, C. Toyokawa, Y. Yalikun, M. Yamada, M. Yamagishi, T. Yamano, A. Yasumoto, Y. Yatomi, M. Yazawa, D. Di Carlo, Y. Hosokawa, S. Uemura, Y. Ozeki and K. Goda, *Cell*, 2018, **175**, 266-276 e213.
6. M. Tanyeri, M. Ranka, N. Sittipolkul and C. M. Schroeder, *Lab Chip*, 2011, **11**, 1786-1794.
7. S. Yamaguchi, A. Ueno, Y. Akiyama and K. Morishima, *Biofabrication*, 2012, **4**, 045005.